# Electronic Supplementary Information

# Nano Cocatalyst-Catalytic System for Boosting Photothermal-Photocatalytic Water Treatment Enabled by Visible LED

Jiaxin Ni[a], Zongsu Wei[c], Aiwen Wang[a], Dongmei Liu[a*], Wei Wang[a], Xiumei Song[a], Zipeng Xing[b*]

[a.] State Key Laboratory of Urban Water Resource and Environment (SKLUWRE), School of Environment, Harbin Institute of Technology, Harbin, 150090, PR China

[b.] Department of Environmental Science, School of Chemistry and Materials Science, Key Laboratory of Functional Inorganic Material Chemistry, Ministry of Education of the People's Republic of China, Heilongjiang University, Harbin 150080, PR China

[c.] Centre for Water Technology (WATEC), Department of Biological and Chemical Engineering, Aarhus University, Universitetsbyen 36, 8000, Aarhus C, Denmark

*Corresponding author: Dongmei Liu; Zipeng Xing

*E-mail: ldm819@126.com; xingzipeng@hlju.edu.cn

Supplementary Material file includes 1 section, 22 figures and 11 tables.

**Table of contents**

**Section 1. Experimental Section**

**Materials**

In this work, all reagents employed in experiments were analytical grade without further purification. Potassium bromide (KBr), polyvinylpyrrolidone (PVP) and tetracycline hydrochloride (TCH) were purchased from Aladdin Reagent Company, China. Bismuth nitrate pentahydrate ($Bi(NO_3)_3 \cdot 5H_2O$), absolute ethanol (EtOH) and ethylene glycol (EG) were purchased from Tianjin Fuyu Fine Chemical Co. Ltd, China. $MoO_3$ and KSCN were purchased from Tianjin Guangfu Fine Chemical Research Institute, China. Deionized water was used throughout all experiments.

**Construction of oxygen vacancies-modified flower-like BiOBr**

Typically, 0.85 g of $Bi(NO_3)_3 \cdot 5H_2O$ was dissolved into a mixed solvent with a volume of 60 mL (the volume ratio of water to EG was 1:5), and an ultrasound treatment was conducted for 30 min. Then, 0.7 g of PVP was dissolved into the solution. After that, 0.2 g of KBr was dissolved with magnetic stirring until the color of the suspension turned to milky white. Next, the mixture was transferred into the autoclave and kept at 160 °C for 12 hours. Finally, the catalyst was obtained after centrifugation and dried overnight. Noted it as FBBov. Besides, the flower-like BiOBr without oxygen vacancies was also prepared (just with no EG addition). Marked the flower-like BiOBr as FBB.

**Synthesis of layered $MoS_2$**

Specifically, 0.3 g of $MoO_3$ and 0.7 g of KSCN were fully ground and then dissolved into 60 mL of DI with a 30 min ultrasonic treatment. Next, the mixture was transferred into the autoclave and kept at 200 °C for 24 hours. Finally, the catalyst was obtained after centrifugation and dried overnight. Noted it as layered $MoS_2$.

**Fabrication of FBBov@MoS₂(1:1) cocatalytic-photocatalytic system**

To be specific, 1.0 g of FBBov was dispersed into a mixed solvent with a volume of 100 mL (the volume ratio of water to ethanol was 4:1), and subsequently 1.0 g of layered $MoS_2$ was added. After a 60 min ultrasonic process, the pH of the mixture was adjusted to a typical value and was kept stirring at room temperature for 6 hours, followed by centrifugation, washing and drying to obtain the target FBBov@MoS₂(1:1) cocatalytic-photocatalytic system. In addition, the quantities of FBBov and layered $MoS_2$ were adjusted to get FBBov@MoS₂(2:1) and FBBov@MoS₂(1:2).

**Characterization**

X-ray diffraction patterns (XRD) were collected by a Bruker D8 Advance XRD with Cu Kα radiation ($\lambda = 0.154060$ nm). Fourier transformed infrared (FT-IR) spectra were recorded on a Perkin Elmer Spectrum One system using KBr as diluents. Scanning electron microscopy (SEM) was performed with a SIGMA 500 operated at an accelerating voltage of 10 or 20 kV. Transmission electron microscopy (TEM) images were obtained with a JEOL 1400 and high-resolution transmission electron microscopy (HRTEM) images were obtained by JEM-2100F instrument with an acceleration voltage of 200 kV. X-ray photoelectron spectroscopy (XPS) were taken on a Thermo

ESCALAB 250 with Al Kα X-ray (hν = 1486.6 eV) radiation and all the binding energies were calibrated using C 1s peak (284.8 eV). Nitrogen adsorption/desorption isotherms were performed on a QuadraSorb SI Instruments. The specific surface area was measured by the Brunauer-Emmett-Teller (BET) method and the pore-size distribution was measured using the density functional theory method. The UV-vis diffuse reflectance spectra (UV-vis DRS) were recorded by a spectrophotometer (Shimadzu UV2550), in which $BaSO_4$ was employed as the background. The photoluminescence (PL) spectra of the samples were measured with a spectrofluorophotometer (LS55 Perkin-Elmer) and the time-resolved fluorescence measurements were recorded on an Edinburgh FLS980. A 3D excitation-emission matrix fluorescence spectrometer (FP6500, JASCO) was used to quantify the fluorescent compounds in the solution. TOC analyzer (5000A, Shimadzu) was used to monitor the total organic carbon (TOC) removal. Thermal images were taken with a thermal imager (Testo Co., Ltd., Testo 865) to perform quantitative analyses of photothermal effect of samples. The light intensity was calibrated using a power meter (PM100D, Thorlabs Inc.) equipped with a thermal sensor (S425C, Thorlabs Inc.). The electron spin resonance (ESR) analysis was conducted with a Bruker A 200s. Transformation products (TPs) of OFL were analyzed by an Agilent 1290 HPLC coupled to a time-of-flight mass spectrometry equipped with electrospray ionization and quadrupole (ESI-Q-TOF-MS, G6540A, Agilent). A volume of 10 μL was injected. A Waters C18 column (3.0 × 100 mm, 2.5 μm particle size) was applied. The binary mobile phase was comprised of 0.5% formic acid aqueous solution (named as solvent

a) and acetonitrile (named as solvent b). The elution process was conducted at a flow rate of 0.2 mL min$^{-1}$. The mass spectra were conducted over m/z range of 50-500 under positive mode electrospray ionization (ESI+). In addition, all statistical analysis relies on IBM SPSS Statistics.20.

**Trapping experiments of radicals and holes**

The trapping experiments were conducted under the similar experimental conditions as previous photocatalytic experiments, except that the specific scavengers were added into the solution before light illumination. The main oxidative species detected by the trapping experiments were·$O_2^-$, ·OH, and holes by using EDTA-2Na (holes scavenger), tertiary butanol (·OH scavenger) and L-ascorbic acid (·$O_2^-$ scavenger), respectively. To emphasized, the concentration of each trapping agents should be kept at 5 mM.

**Cyclic degradation process**

After each photocatalytic degradation process, the photocatalyst was centrifuged and then washed with DI water and absolute ethanol for several times. The cleaned photocatalyst was dried, collected and accurately weighed. After that, filled the mass of catalyst to the initial 20 mg and the next photocatalytic cycle process was carried out.

**Fig. S1.** Photograph of the photochemical reaction system.
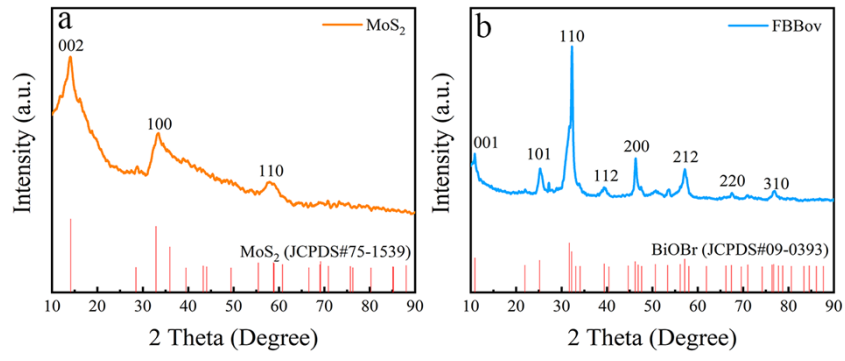
**Fig. S2.** XRD patterns of (a) MoS$_2$ and (b) FBBov.
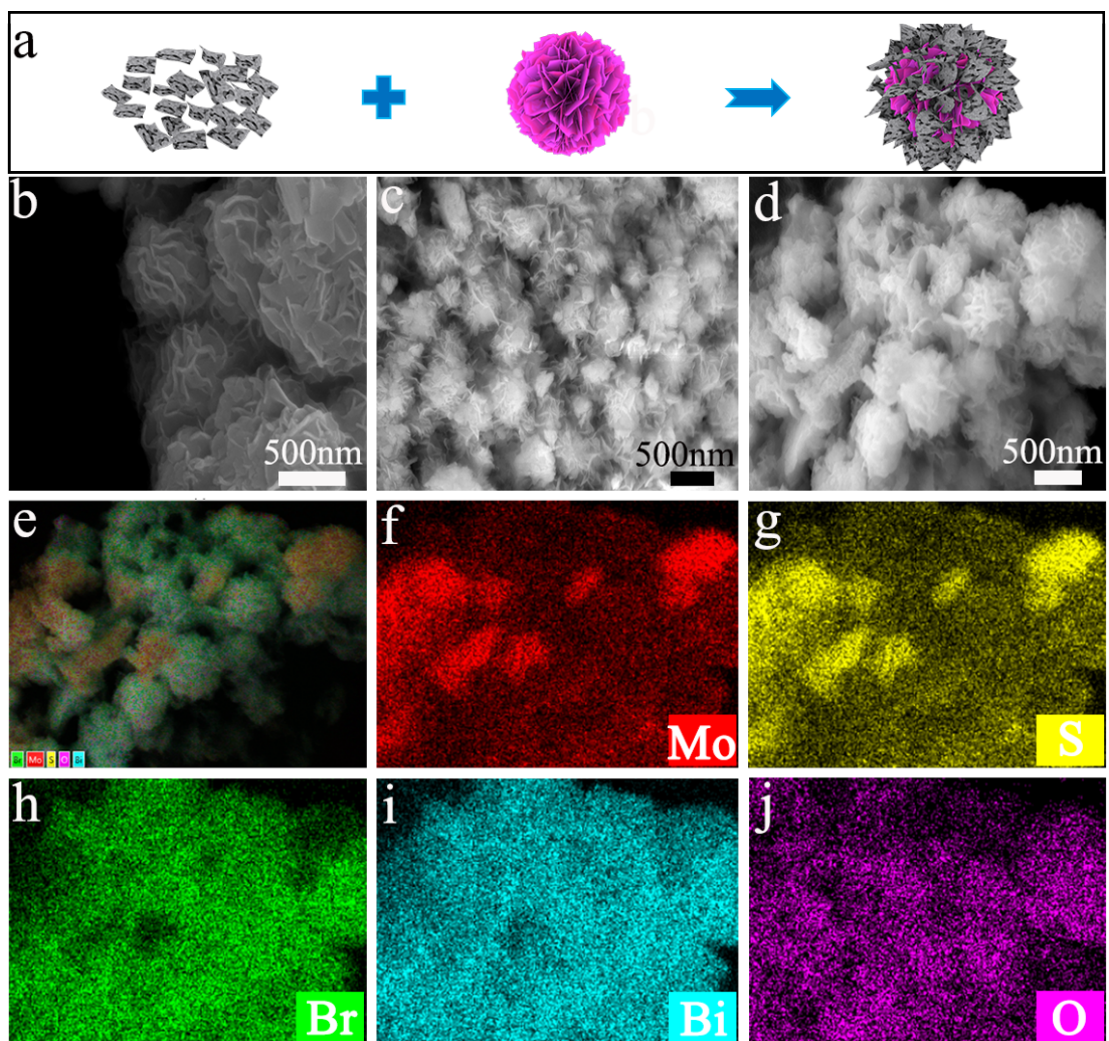
**Fig. S3.** (a) 3D schematic illustration of FBBov@MoS$_2$(1:1). SEM images of (b) FBBov, (c) MoS$_2$ and (d) FBBov@MoS$_2$(1:1). (e~j) SEM-EDS analysis for FBBov@MoS$_2$(1:1).
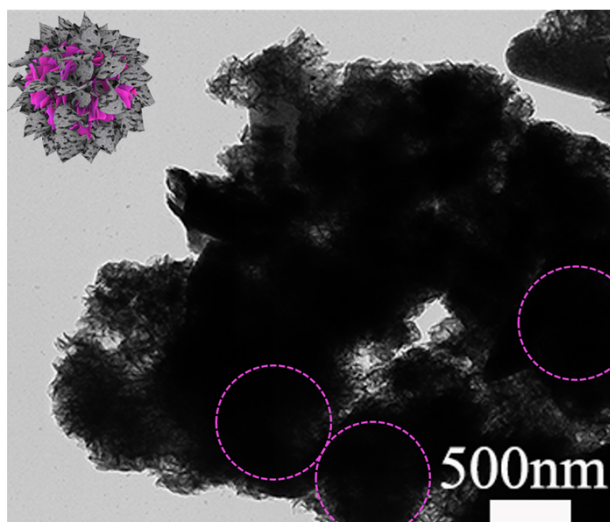
**Fig. S4.** TEM images of FBBov@MoS$_2$(1:1).
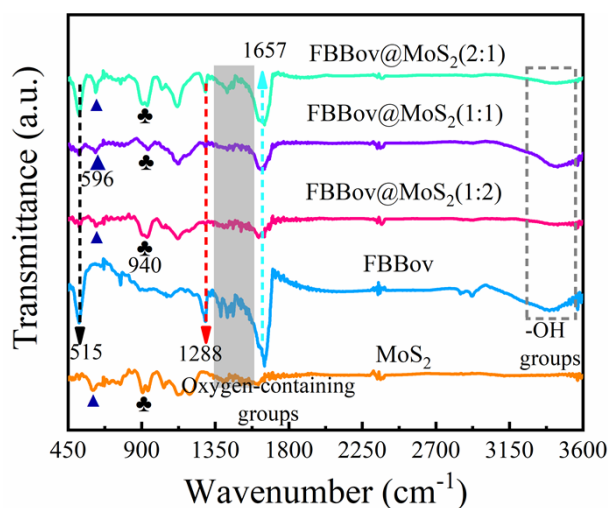
**Fig. S5.** FT-IR spectra of MoS$_2$, FBBov, FBBov@MoS$_2$(2:1), FBBov@MoS$_2$(1:1) and FBBov@MoS$_2$(1:2), respectively.

FT-IR is utilized to investigate the surface structure of photocatalysts (Fig S5). The vibration peaks of MoS$_2$ at 596 cm$^{-1}$ and 940 cm$^{-1}$ may be attributed to the S-Mo and Mo-O bonds [1]. In terms of the FBBov spectrum, a distinct peak at 1657 cm$^{-1}$ is ascribed to the O-H bending vibration [2], while another peak at 1288 cm$^{-1}$ is related to the asymmetric Bi-Br stretching vibration. Moreover, the detection of a prominent absorption peak at 515 cm$^{-1}$ suggests the crystallization of BiOBr [3]. Besides, the typical peaks of MoS$_2$ and FBBov could be found in FBBov@MoS$_2$(1:1), indicating their successful composition.
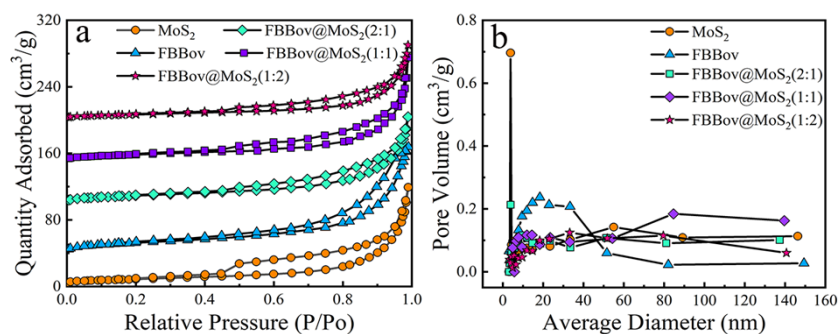
**Fig. S6.** (a) $N_2$-adsorption/desorption isotherm curves and (b) pore size distribution plots of $MoS_2$, FBBov, FBBov@$MoS_2$(2:1), FBBov@$MoS_2$(1:1) and FBBov@$MoS_2$(1:2), respectively.

$N_2$ adsorption-desorption isotherms are also carried out. According to the IUPAC classification, mesoporous could be observed in all catalysts, as indicated in Fig. S6a, and catalysts might display irregular pore structures, which are connected to the pore size distribution in Fig. S6b. As demonstrated in Table S1, the BET surface areas of FBBov, $MoS_2$, FBBov@$MoS_2$(1:2), FBBov@$MoS_2$(1:1), and FBBov@$MoS_2$(2:1) are 61.1, 74.5, 53.7, 50.9, and 49.6 $m^2 \cdot g^{-1}$, respectively.
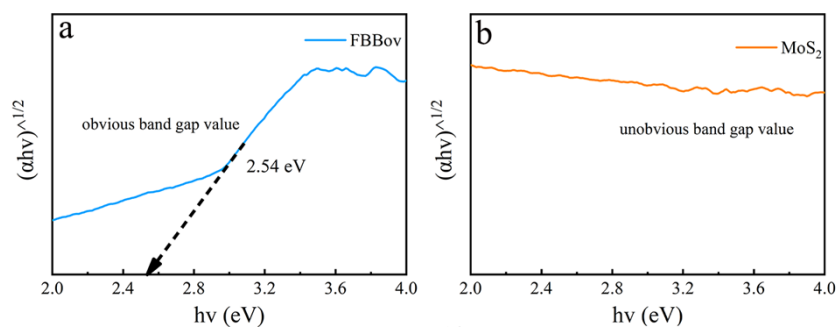
**Fig. S7.** Determination of the indirect interband transition energies of (a) FBBov and (b) MoS$_2$.
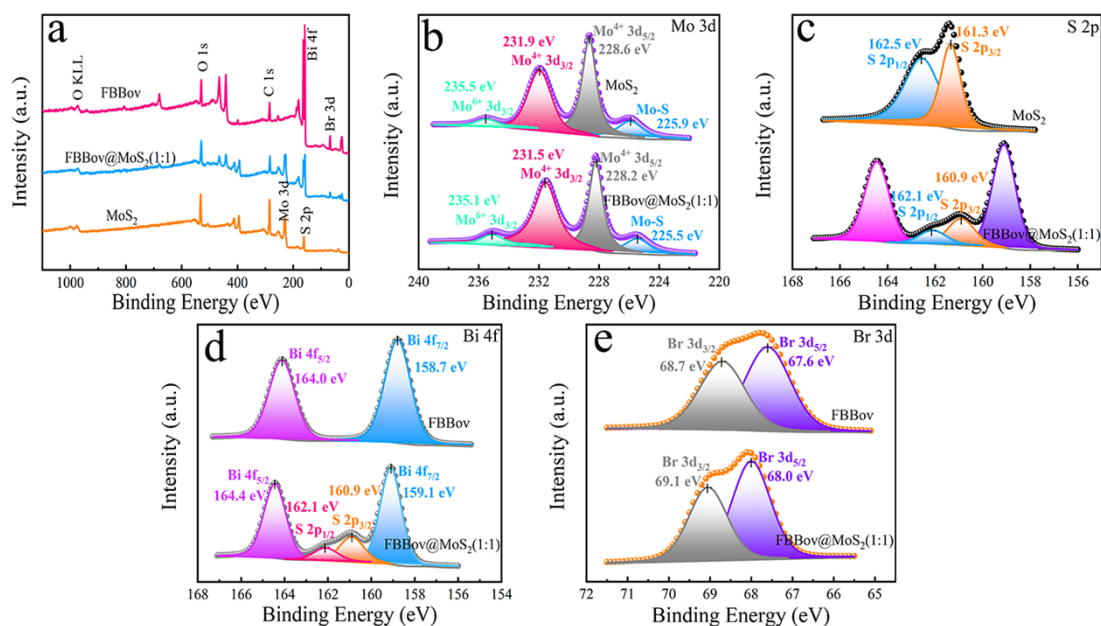
**Fig. S8.** (a) Full XPS spectrum and high-resolution spectra of catalysts: (b) Mo 3d, (c) S 2p, (d) Bi 4f, and (e) Br 3d.

XPS is performed to investigate the elemental composition, valence distribution, and potential modes of electron transfer. The XPS survey spectra of FBBov, $MoS_2$ and FBBov@$MoS_2$(1:1) are presented in Fig. S8a, which exhibits the presence of Bi, O, Br, Mo and S elements. In the meantime, the same positions of each element further prove the effective construction of FBBov@$MoS_2$(1:1). Additionally, the valence states and bonding modes of each element are confirmed. In Fig. S8b, three peaks at 225.9, 228.6, and 231.9 eV, could be respectively attributed to Mo-S, $Mo^{4+}$ $3d_{5/2}$, and $Mo^{4+}$ $3d_{3/2}$ in $MoS_2$ [4], demonstrating the successful synthesis of $MoS_2$. Meanwhile, the peak from the $MoO_3$ phase of $Mo^{6+}$ $3d_{3/2}$ is exhibited nearby, which is similar to the FT-IR result, generating from an oxidized effect [1]. For the high-resolution XPS spectra of S 2p (Fig. S8c), energy values of 161.3 and 162.5 eV are compatible with S $2p_{3/2}$ and S $2p_{1/2}$ of Mo-S bonds [1, 4], respectively. Bi in Fig. S8d is deconvolved into two peaks at

16

roughly 158.7 and 164.0 eV, which are labeled as Bi $4f_{7/2}$ and Bi $4f_{5/2}$ [6]. Two prominent peaks in the Br 3d spectrum (Fig. S8e) are respectively attributed to the Br $3d_{5/2}$ and Br $3d_{3/2}$. To emphasize, peaks of Bi 4f and Br 3d in FBBov@$MoS_2$(1:1) move 0.4 eV to higher binding energy, whereas all peaks of Mo 3d and S 2p shift 0.4 eV to lower binding energy. This implies that the chemical environment has altered as a consequence of charge redistribution induced by changing surface-electron density [7, 8], which might be related to the creation of the cocatalyst-photocatalytic system.
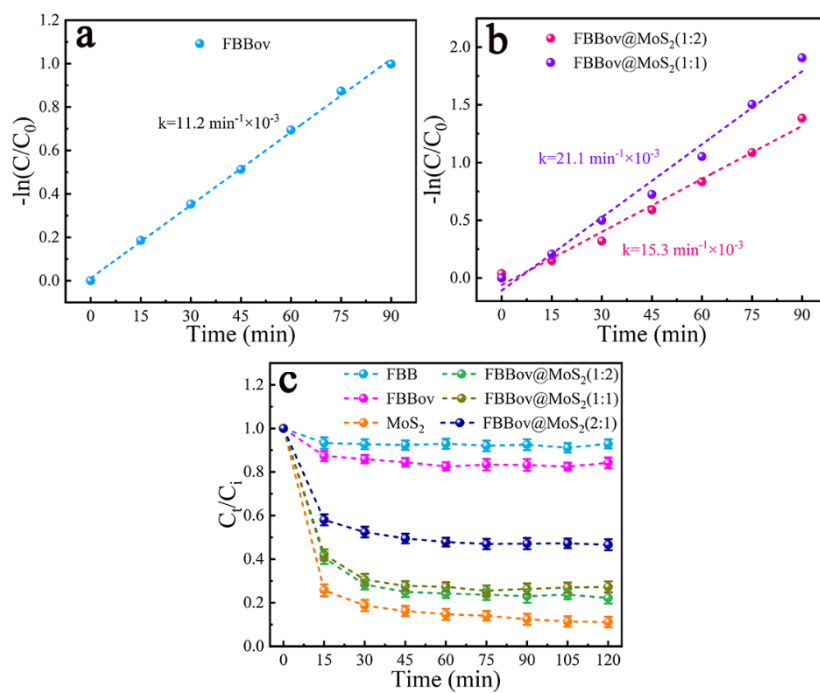
**Fig. S9.** (a b) Variations of -ln (C/C$_0$) versus LED visible-light irradiation time via samples and (c) Dark adsorption of TCH with six samples.
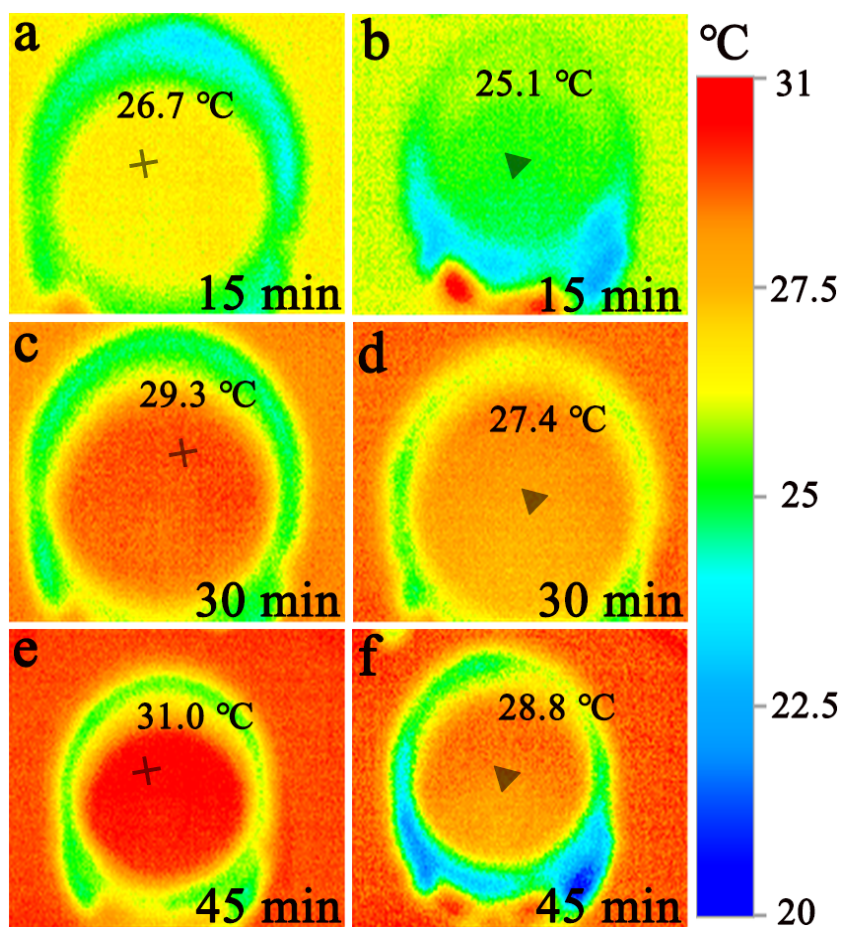
**Fig. S10.** The IR images of the photocatalytic system (a, c, e) with or (b, d, f) without FBBov@MoS$_2$(1:1) at different reaction times, respectively.
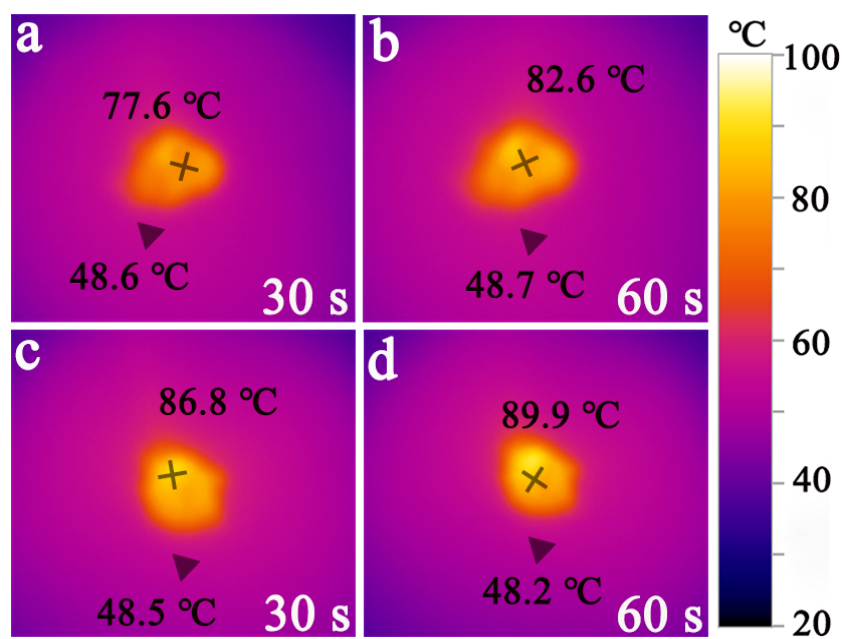
**Fig. S11.** The IR images of (a~b) FBBov@MoS$_2$(2:1) and (c~d) FBBov@MoS$_2$(1:2) with different irradiation times, respectively.
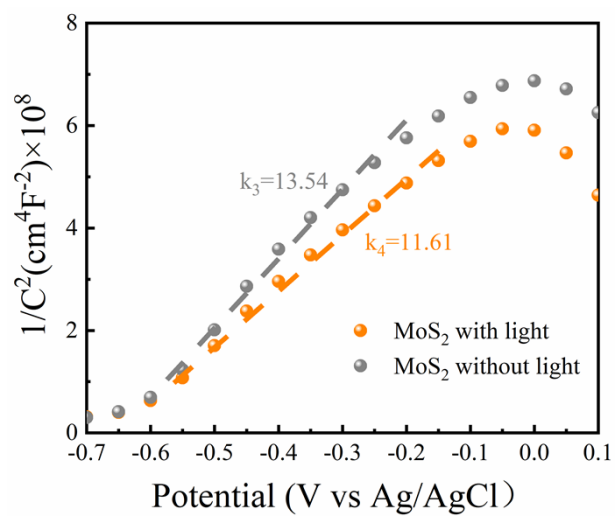
**Fig. S12.** Mott-Schottky plots of MoS$_2$.
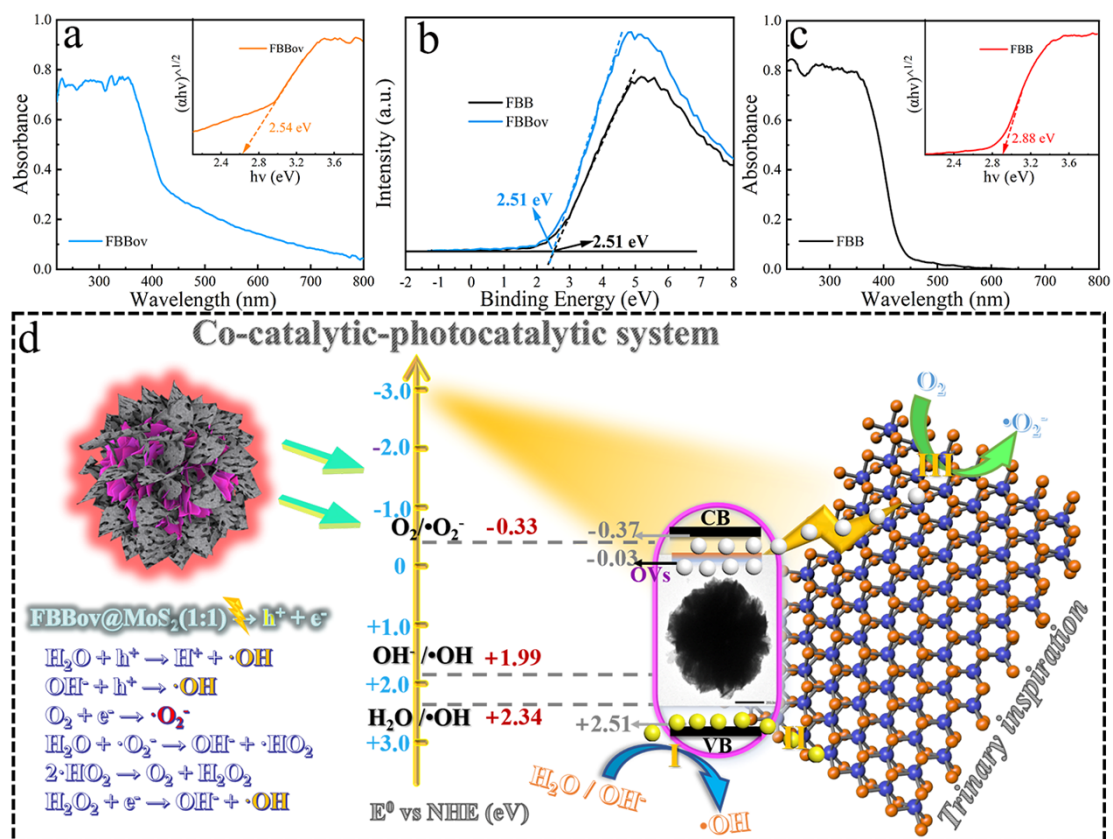
**Fig. S13.** (a) UV-visible diffuse reflectance spectrum of FBBov. (b) VB-XPS of FBBov and FBB.

(c) UV-visible diffuse reflectance spectrum of FBB. (d) Energy band schematic diagram of the co-catalytic-photocatalytic system.
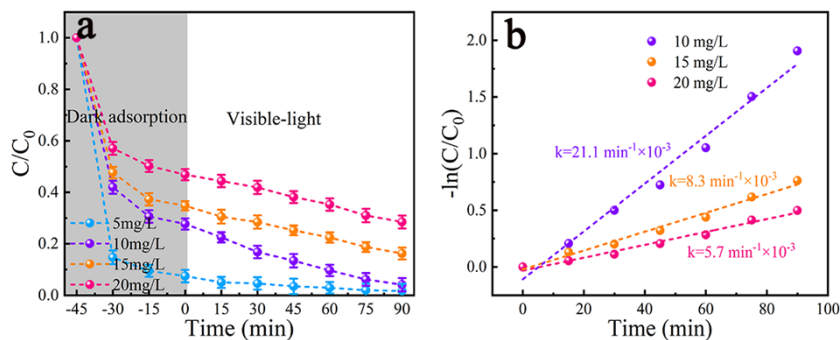
**Fig. S14.** (a) Effect of initial TCH concentration via FBBovMoS$_2$(1:1) on photocatalysis and (b) variations of -ln(C/C$_0$) versus LED visible-light irradiation time via concentrations.

The effect of TCH concentrations is shown in Fig. S14a. At low concentrations, FBBovMoS$_2$(1:1) can remove most of TCH via adsorption. At 5 mg/L, 92.5 % of TCH can be removed by adsorption within 45 min. Whereas, the total removal rate of TCH continues to decrease as the concentration improves, which are 95.8 %, 83.8 % and 71.5 % corresponding to 10, 15 and 20 mg/L in 135 min. Photocatalytic kinetic analysis of 10-20 mg/L experiments is performed, as indicated in Fig. S14b. As the initial TCH concentration increases, the k is reduced from 21.1 min$^{-1}$×10$^{-3}$ to 5.7 min$^{-1}$×10$^{-3}$. However, due to the low-energy consumption (Table S6), it is reasonable to anticipate that FBBov@MoS$_2$(1:1) can entirely eliminate TCH by extending the reaction time.
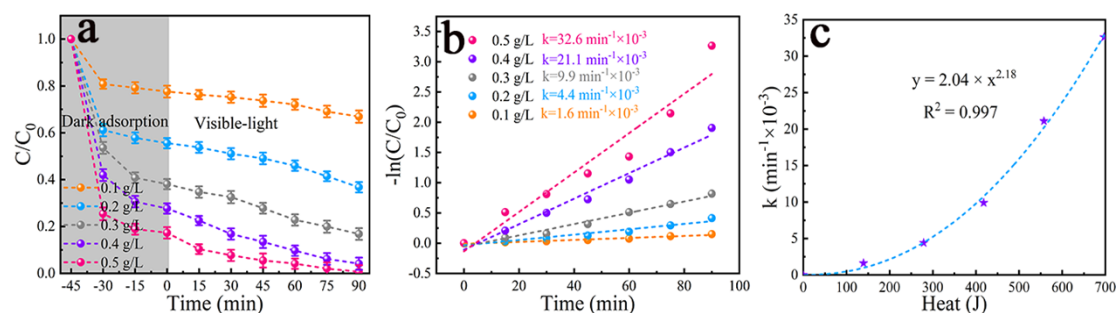
**Fig. S15.** (a) Effect of dosage via FBBovMoS$_2$(1:1) on photocatalysis. (b) Variations of -ln (C/C$_0$) versus LED visible-light irradiation time via dosages. (c) Fitting curve of heat and k.

Furthermore, the dosage impact of FBBovMoS$_2$(1:1) is depicted in Fig. S15a. During the experiment, the explored dosage range is 0.1-0.5 g/L when the TCH concentration is 10 mg/L. Corresponding results reveal that the larger the amount of FBBov@MoS$_2$(1:1), the higher the removal rate. At 0.5 g/L, the TCH removal rate reaches 95.9 % at 60 min of photocatalysis. In kinetic analysis, the response k varies across the dosage meanwhile its improvement increases with the change of dosage (Fig. S15b). According to the proposed FBBov@MoS$_2$(1:1) photothermal enrichment equation, the generated heat of each dosage system at 90 min photocatalysis is calculated as 139.4, 278.8, 418.1, 557.5 and 696.9 J, respectively. Heat and k have an exponential relationship instead of a linear dependency (Fig. S15c), indicating that the k may be further increased through heat generated by FBBov@MoS$_2$(1:1). This also confirms the promotion of the photothermal effect in our experiment. Therefore, whenever FBBovMoS$_2$(1:1) is used for removing refractory contaminants, the efficiency could be enhanced by increasing the dosage, not only resulting from additional ROSs, but also owing to the increased heat.
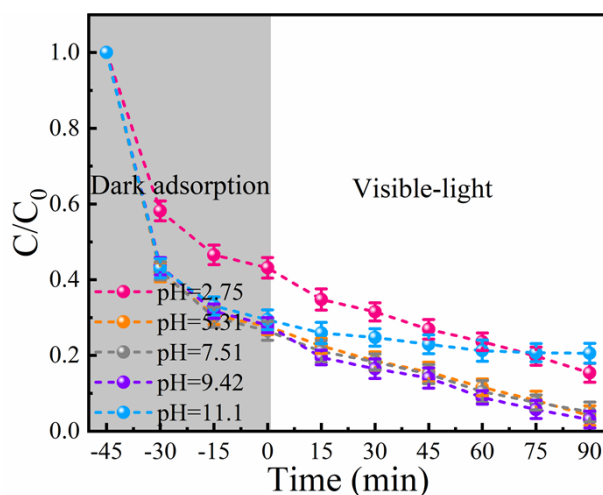
**Fig. S16.** Effect of initial pH via FBBovMoS$_2$(1:1) on photocatalysis.

During photocatalytic processes, pH tends to influence the surface charge distribution and the formation of ROSs, affecting the activity of photocatalysts [9]. As a consequence, TCH removal processes at different pH (2.75, 5.31, 7.51, 9.42, 11.10) are investigated, as shown in Fig. S16. When the pH is 5.31, 7.51 or 9.42, the degradation curves are comparable. Herein, the statistical method One-way ANOVA is employed to analyze their differences in detail, as shown in Table S7. The difference among three groups is not statistically significant (Sig.>0.05). In other words, the activity of FBBovMoS$_2$(1:1) would not be affected in the pH range of 5.31-9.42. For the degradation process under acidic conditions (pH=2.75), FBBovMoS$_2$(1:1) shows a different effect. The TCH removal rate within dark adsorption is 56.8 %, which is 15.2 % lower than that at pH=9.42. Meanwhile, the difference between the two processes at each point is similar so additional statistical analysis is also performed (Table S8), demonstrating the linear correlation between the two pH values. Therefore, the removal difference between pH 9.42 and 2.75 could be considered originating from the

adsorption process. Under strongly acidic circumstances, the $h^+$-dominated photocatalysis of $FBBovMoS_2$(1:1) is not affected, whereas excess hydrogen ions change the surface charge distribution of $FBBovMoS_2$(1:1), inhibiting the adsorption performance. For strong alkali conditions, results are quite different. At pH=11.1, the adsorption process of $FBBovMoS_2$(1:1) is not excessively disturbed with 70.6 % removal of TCH. However, the photocatalytic process is severely suppressed. The total removal rate of TCH is only 79.4 %, which indicates only 8.8 % of TCH is removed in 90 min photocatalysis. This may be caused by the quenching of ROSs [10]. Under alkaline conditions, $h^+$ could react with $OH^-$, losing their oxidability.
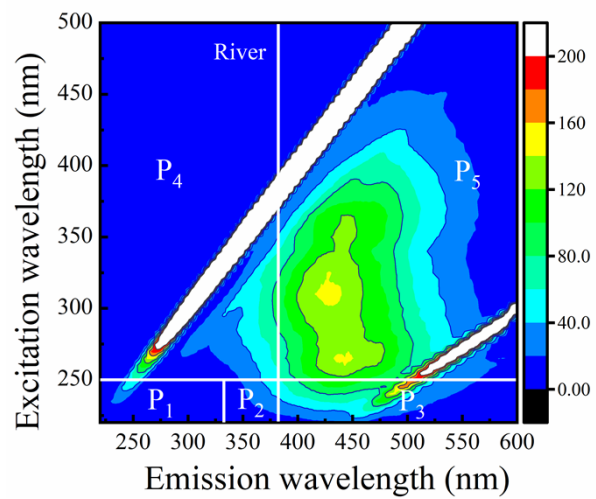
**Fig. S17.** Three-dimensional EEM spectrum of original river water.
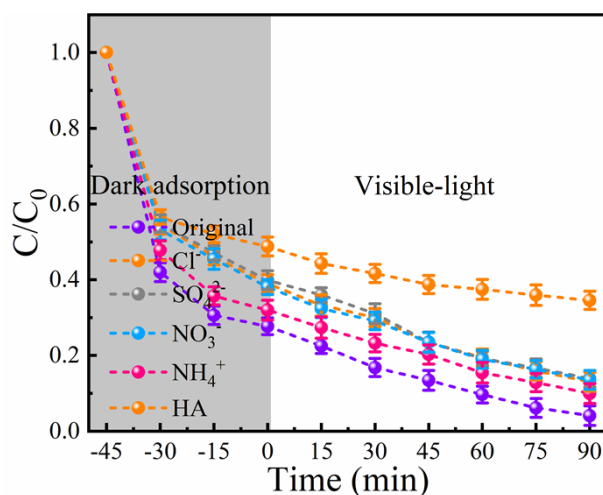
**Fig. S18.** Effect of interfering ions via FBBovMoS$_2$(1:1) on photocatalysis.

Ions in water often interfere with AOPs [11]. Therefore, the impact of Cl$^-$, SO$_4^{2-}$, NO$_3^-$ and NH$_4^+$ on FBBovMoS$_2$(1:1) is studied with their concentration of 10 mM, as shown in Fig. S18. Generally, the interfering ions inhibit the removal of TCH, which are 61.0 %, 60.1 %, 61.9 % and 68.0 % within adsorption while 86.9 %, 86.1 %, 86.5 % and 90.0 % in 135 min. A statistical method is conducted to compare the differences among ion groups and the original one (Table S9). The linear correlation among each ion group and the original one is significant, so the difference in TCH removal rate is considered to cause by adsorption. In other words, during the concentration range we explored, the presence of interfering ions mostly influences the adsorption efficiency of FBBov@MoS$_2$(1:1) without much interference in photocatalysis. This is because ions in the solution are adsorbed on the surface of FBBovMoS$_2$(1:1) to occupy part of the adsorption sites, affecting the adsorption removal of TCH, whereas the photocatalytic degradation process is not adversely impacted. Furthermore, humic acid (HA) is selected as a representative natural organic matter (NOM) for exploration. The

HA affects both the adsorption and photocatalytic processes of FBBovMoS$_2$(1:1), resulting in only 65.5 % removal of TCH at 135 min. It is thought that the NOMs might compete with TCH and consume a considerable quantity of SOSs, hence affecting the photocatalytic degradation process of TCH. Subsequent actual water degradation also verifies our conclusion.
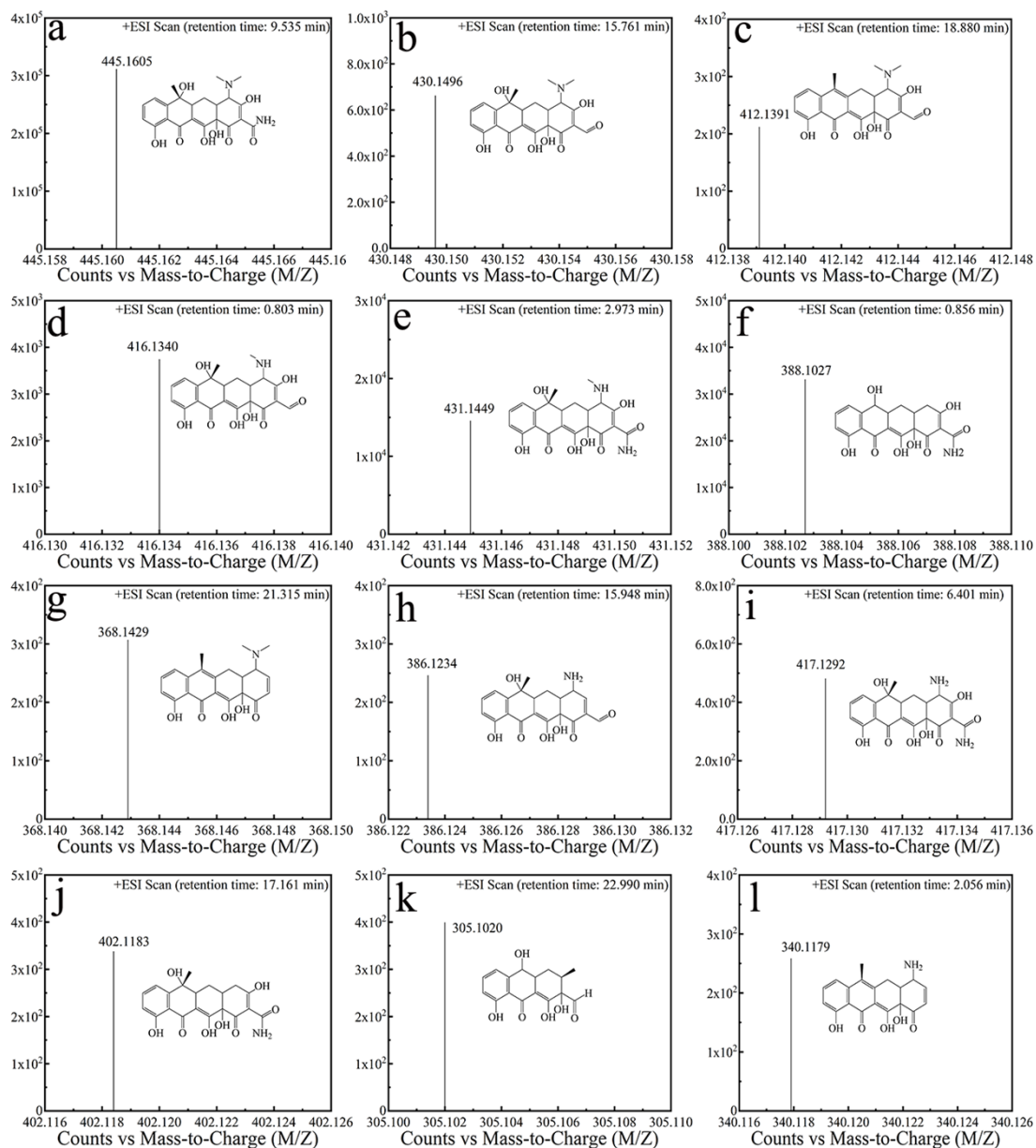
**Fig. S19.** MS spectrum of intermediate products with proposed fragmentation pathway.
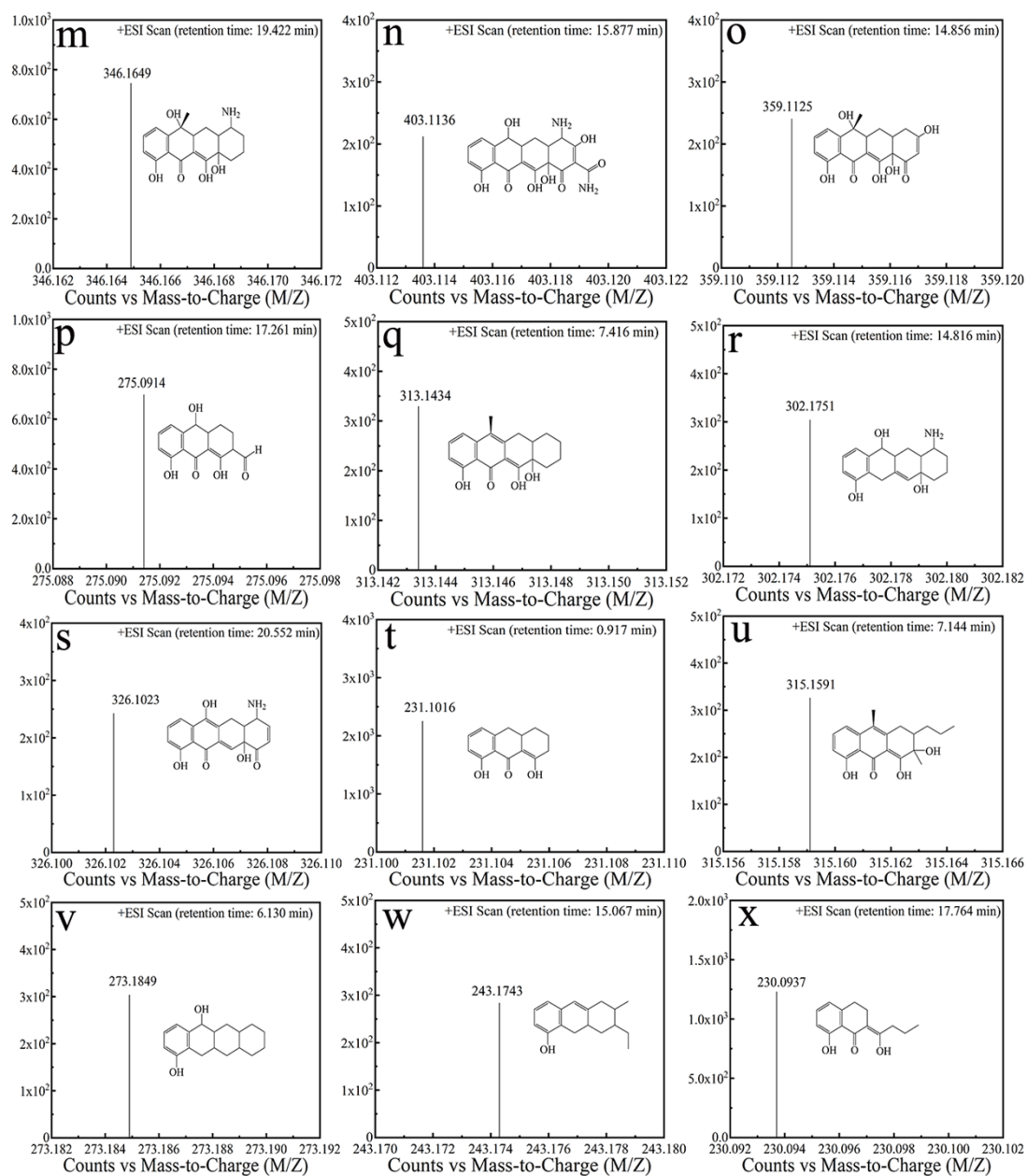
**Fig. S20.** MS spectrum of intermediate products with proposed fragmentation pathway.
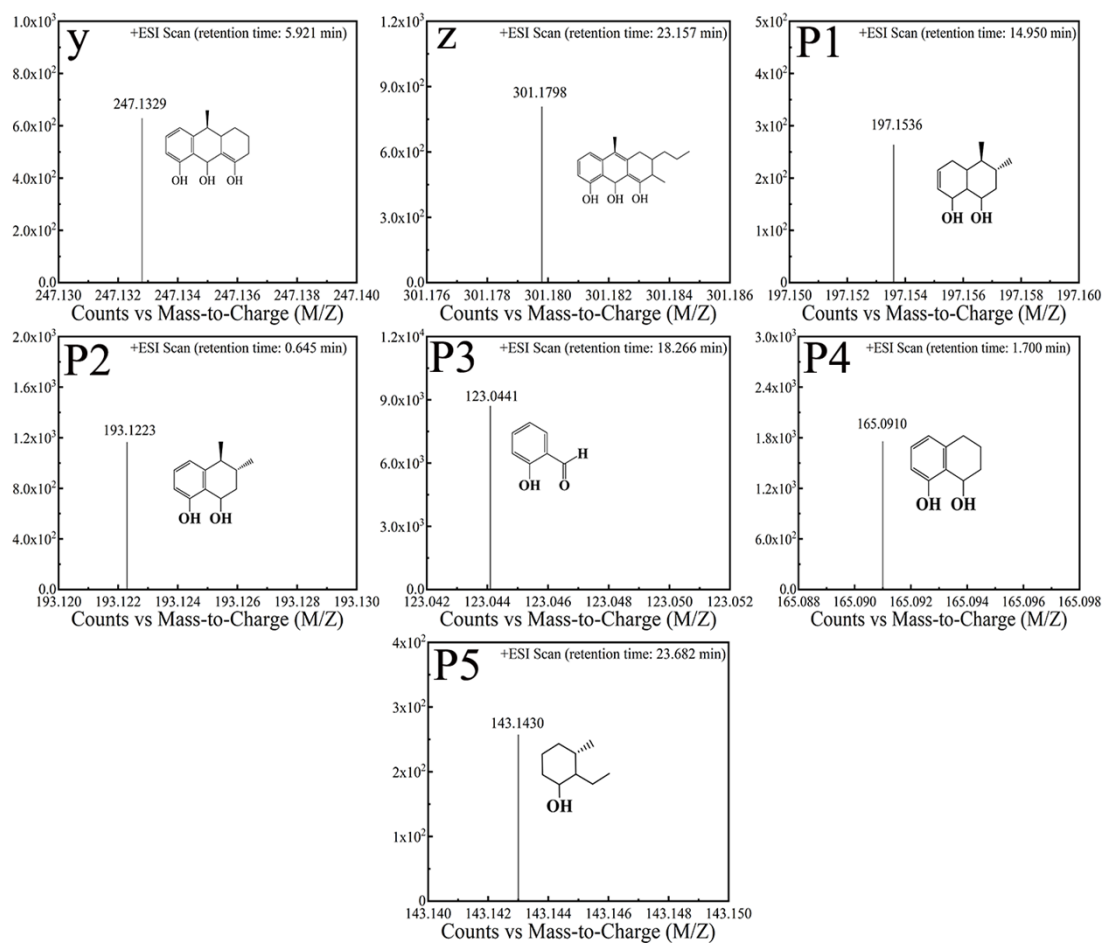
**Fig. S21.** MS spectrum of intermediate products with proposed fragmentation pathway.
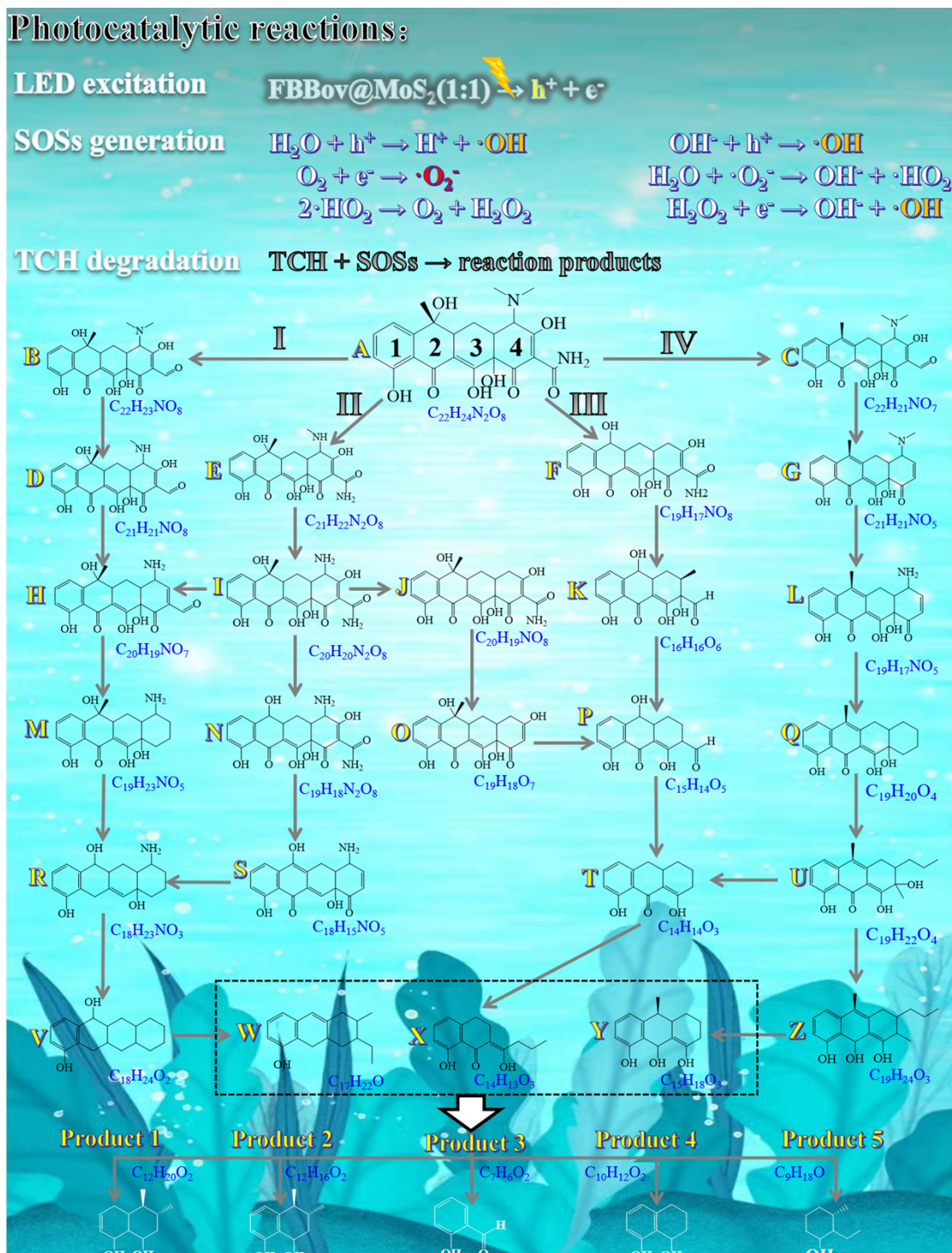
**Fig. S22.** Proposed pathways for degradation of TCH by FBBov@MoS$_2$(1:1) under visible LED.

Furthermore, intermediate products are identified by LC-MS meanwhile the degradation mechanism of TCH is shown in Fig. S22. Fragmentation analysis is performed using Agilent Mass Hunter software B.08.00, as demonstrated in Fig. S19-

21. In combination with relevant literature [12-14] and the bond-breaking mode of TCH, the structure of intermediates is shown in Table S11. The degradation process of TCH is completed by three SOSs dominated by $\cdot O_2^-$, h+ and $\cdot OH$, which can be roughly summarized into four pathways. Pathway I: Ring 4 of TCH is assaulted by SOSs, shedding $-NH_2$ and $-CH_3$ sequentially to get fragments B and D. Then, $-CH_3$ and $-OH$ simultaneously fall off to generate H. Following that, $-C=O$ is attacked and $-C=C-$ in ring 4 is fractured, leading in fragment M. Next, substituents on ring 2 and 3 are continually oxidized, resulting in fragment R and V. Pathway II: Two $-CH_3$ are consecutively dropped from TCH to obtain fragment E and I. As a key intermediate, fragment I could be converted into H, J and N by shedding $-OH$, $-NH_2$ and $-CH_3$, respectively. Then, fragment N is attacked by SOSs and the amide group and $-OH$ fall off to form S, which eventually becomes R. Pathway III: To obtain F, $-N(CH_3)_2$ in ring 4 and $-OH$ in ring 2 are simultaneously oxidized. Next, fragment F is attacked and ring 4 is opened to become K. After removing $-OH$ and $-CH=O$, fragment K turns into P and T, respectively. Pathway IV: $-OH$ and $-NH_2$ are respectively attacked in ring 2 and 4 to get C. Subsequently, ring 4 further sheds $-C=O$ and $-OH$ to generate fragment G. Following that, another two $-CH_3$ are assaulted by SOSs, forming L. Fragment L could be further oxidized to produce Q and U, which could be followed by T and Z. Among these four pathways, W, X and Y are critical intermediate products, which would be further oxidized into Product 1-5 and eventually decomposed to $CO_2$, $H_2O$ and other inorganic substances.

**Table S1**. Parameters obtained from $N_2$ desorption isotherm measurements.

| Samples | BET surface area ($m^2 \cdot g^{-1}$) | Pore size (nm) | Pore volume ($cm^3 \cdot g^{-1}$) |
|---|---|---|---|
| FBBov | 61.1 | 3.06 | 0.20 |
| $MoS_2$ | 74.5 | 3.81 | 0.20 |
| FBBov@$MoS_2$(1:2) | 53.7 | 3.82 | 0.20 |
| FBBov@$MoS_2$(1:1) | 50.9 | 3.82 | 0.20 |
| FBBov@$MoS_2$(2:1) | 49.6 | 3.83 | 0.17 |

**Table S2.** Exponential decay-fitted parameters of fluorescence lifetime of samples.

| Samples | $A_1$ | $\tau_1$ (ns) | $A_2$ | $\tau_2$ (ns) | $\tau_{avg}$ (ns) |
|---|---|---|---|---|---|
| FBBov | 6794.96 | 0.68 | 806.15 | 3.36 | 1.67 |
| MoS$_2$ | 6367.63 | 0.75 | 469.07 | 4.39 | 1.85 |
| FBBov@MoS$_2$(1:1) | 3047.23 | 1.09 | 365.70 | 5.64 | 2.83 |

The $\tau_1$ or $\tau_2$ is lifetime while $A_1$ or $A_2$ is magnitude.

**Table S3.** Comparison of photocatalytic performance on TC among FBBov@MoS$_2$(1:1) and other catalysts.

| Photocatalysts | Catalyst dosage (g·L$^{-1}$) | Light source | Removal rate | Rate constant (min$^{-1}$) | Ref. |
|---|---|---|---|---|---|
| FBBov/Ag/UCN | 1.0 | 300 W Xe lamp ($\lambda$>420 nm) | 91.7% (60 min) | 0.0338 | Previous work |
| Ba/g-C$_3$N$_4$ | 1.0 | 150 W Xe lamp ($\lambda$>400 nm) | 69.6% (120min) | 0.0088 | [15] |
| Au/g-C$_3$N$_4$/CeO$_2$ | 0.4 | 500 W Xe lamp ($\lambda$>400 nm) | 95.1% (150 min) | 0.0200 | [16] |
| TiO$_2$-BiOBr - sepiolite | 0.5 | 400 W Xe lamp ($\lambda$>420 nm) | 93% (240min) | 0.0076 | [17] |
| BiOCl@CeO$_2$ | 0.5 | 300 W Xe lamp ($\lambda$>420 nm) | 90% (120 min) | 0.0145 | [18] |
| Ag/AgCl/BiVO$_4$ | 1.0 | 1000 W Xe lamp ($\lambda$>420 nm) | 97.6% (120 min) | 0.0294 | [19] |
| Polyaniline/Perylene diimide (PANI/PDI) | 0.5 | 5 W LED lamp ($\lambda$>420 nm) | 70% (120 min) | 0.0088 | [20] |
| perylene diimide (PDI) | 0.5 | 5 W LED lamp ($\lambda$>420 nm) | 80% (150 min) | 0.0075 | [21] |
| FBBov@MoS$_2$ (1:1) | 0.4 | 5 W LED lamp ($\lambda$>420 nm) | 95.9% (135 min) | 0.0211 | This work |

**Table S4**. Energy comparison of previous work versus current work.

| Index | Comparison | |
|---|---|---|
| | Previous work | Present work |
| Catalyst cost | approximately equal | |
| Visible light | long-arc Xe lamp | LED |
| Number of channels | 9 | 9 |
| Total power (W) | 300 | 5×9 |
| Irradiation time (min) | 60 | 90 |
| Energy consumption (kW·h) | 0.3 | 0.0675 |
| Antibiotic removal rate (%) | 91.7 | 95.8 |
| TOC removal rate (%) | 56.2 | 62.9 |
| Dosage (g/L) | 1.0 | 0.2 |

**Table S5**. TCH removal rates by $MoS_2$ with/without visible light.

| Time (min) | Removal rate (%) | |
| --- | --- | --- |
| | With light | Without light |
| 15 | 74.3 | 75.6 |
| 30 | 81.3 | 81.4 |
| 45 | 83.8 | 84.1 |
| 60 | 86.0 | 86.2 |
| 75 | 86.7 | 86.9 |
| 90 | 87.9 | 88.1 |

**Table S6**. Information got from Paired-sample T test.

| Paired-sample T test | 95% Confidence Interval of the Difference | | t | df | Sig. (2-tailed) |
| --- | --- | --- | --- | --- | --- |
| | Lower | Upper | | | |
| Light on/off | -0.73422 | 0.07708 | 1.982 | 6 | 0.095 |

**Table S7**. Information got from One-way ANOVA for multiple Comparisons.

| One-way ANOVA | Samples | | Sig. | 95% Confidence Interval | | Mean Difference | Std. Error |
|---|---|---|---|---|---|---|---|
| | | | | Lower | Upper | | |
| LSD | pH=5.31 | pH=7.51 | 0.973 | -0.2526 | 0.2612 | 0.00426 | 0.12520 |
| | | pH=9.42 | 0.938 | -0.2471 | 0.2667 | 0.00978 | 0.12520 |
| | pH=7.51 | pH=5.31 | 0.973 | -0.2612 | 0.2526 | -0.00426 | 0.12520 |
| | | pH=9.42 | 0.965 | -0.2514 | 0.2624 | 0.00552 | 0.12520 |
| | pH=9.42 | pH=5.31 | 0.938 | -0.2667 | 0.2471 | -0.00978 | 0.12520 |
| | | pH=7.51 | 0.965 | -0.2624 | 0.2514 | -0.00552 | 0.12520 |

**Table S8**. Information got from Correlation analysis.

| Correlations | Std. Deviation | Covariance | Sig. (2-tailed) | Pearson Correlation |
|---|---|---|---|---|
| pH=2.75 | 0.12520 | 0.009 | 0.000 | 0.995 |
| pH=9.42 | 0.12520 | 0.008 | | |

**Table S9**. Information got from Correlation analysis.

| Correlations | | Cl⁻ | SO₄²⁻ | NO₃⁻ | NH₄⁺ |
|---|---|---|---|---|---|
| Original | Std. Deviation | 0.09544 | 0.10024 | 0.08998 | 0.07978 |
| | Covariance | 0.008 | 0.009 | 0.009 | 0.007 |
| | Sig. (2-tailed) | 0.993 | 0.991 | 0.994 | 0.996 |
| | Pearson Correlation | 0.000 | 0.000 | 0.000 | 0.000 |

**Table S10**. Information about regions of 3D-EEM spectrum.

| Region | Range (X/Y) | Compounds |
|--------|-------------|-----------|
| $P_1$ | 200-330/200-250 nm | Tyrosine-like substances |
| $P_2$ | 330-380/200-250 nm | Tryptophan-like substances |
| $P_3$ | 380-600/200-250 nm | Fulvic acid-like substances |
| $P_4$ | 200-380/250-500 nm | Soluble microbial by-product-like substances |
| $P_5$ | 380-600/250-500 nm | Humic acid-like substances |

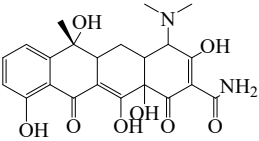**Table S11.** Proposed degradation products of TCH by FBBov@MoS$_2$(1:1).
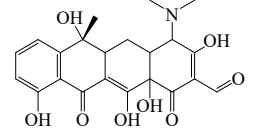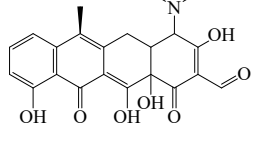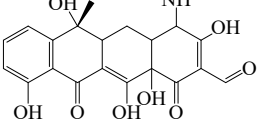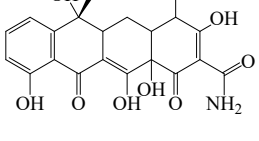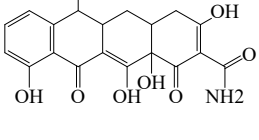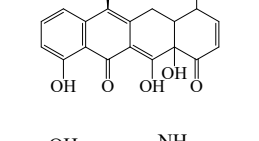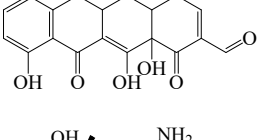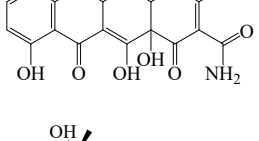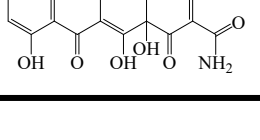
| Formula | [M+H]$^+$ | M/Z | Molecular mass | Proposed structure |
|---|---|---|---|---|
| A C$_{22}$H$_{24}$N$_2$O$_8$ | 445.1605 | 444.15 | 444.44 |  |
| B C$_{22}$H$_{23}$NO$_8$ | 430.1496 | 429.14 | 429.43 |  |
| C C$_{22}$H$_{21}$NO$_7$ | 412.1391 | 411.13 | 411.41 |  |
| D C$_{21}$H$_{21}$NO$_8$ | 416.1340 | 415.13 | 415.40 |  |
| E C$_{21}$H$_{22}$N$_2$O$_8$ | 431.1449 | 430.14 | 430.41 |  |
| F C$_{19}$H$_{17}$NO$_8$ | 388.1027 | 387.10 | 387.34 |  |
| G C$_{21}$H$_{21}$NO$_5$ | 368.1429 | 367.14 | 367.40 |  |
| H C$_{20}$H$_{19}$NO$_7$ | 386.1234 | 385.12 | 385.37 |  |
| I C$_{20}$H$_{20}$N$_2$O$_8$ | 417.1292 | 416.12 | 416.39 |  |
| J C$_{20}$H$_{19}$NO$_8$ | 402.1183 | 401.11 | 401.37 |  |

**Table S11.** (Continued Table)

| Formula | $[M+H]^+$ | M/Z | Molecular mass | Proposed structure |
|---|---|---|---|---|
| K $C_{16}H_{16}O_6$ | 305.1020 | 304.09 | 304.30 |  |
| L $C_{19}H_{17}NO_5$ | 340.1179 | 339.11 | 339.35 |  |
| M $C_{19}H_{23}NO_5$ | 346.1649 | 345.16 | 345.40 |  |
| N $C_{19}H_{18}N_2O_8$ | 403.1136 | 402.11 | 402.36 |  |
| O $C_{19}H_{18}O_7$ | 359.1125 | 358.11 | 358.35 |  |
| P $C_{15}H_{14}O_5$ | 275.0914 | 274.08 | 274.27 |  |
| Q $C_{19}H_{20}O_4$ | 313.1434 | 312.14 | 312.37 |  |
| R $C_{18}H_{23}NO_3$ | 302.1751 | 301.17 | 301.39 |  |
| S $C_{18}H_{15}NO_5$ | 326.1023 | 325.10 | 325.32 |  |
| T $C_{14}H_{14}O_3$ | 231.1016 | 230.09 | 230.26 |  |

**Table S11.** (Continued Table)

| Formula | $[M+H]^+$ | M/Z | Molecular mass | Proposed structure |
|---|---|---|---|---|
| U $C_{19}H_{22}O_4$ | 315.1591 | 314.15 | 314.38 |  |
| V $C_{18}H_{24}O_2$ | 273.1849 | 272.18 | 272.39 |  |
| W $C_{17}H_{22}O$ | 243.1743 | 242.17 | 242.36 |  |
| X $C_{14}H_{13}O_3$ | 230.0937 | 232.11 | 232.28 |  |
| Y $C_{15}H_{18}O_3$ | 247.1329 | 246.13 | 246.31 |  |
| Z $C_{19}H_{24}O_3$ | 301.1798 | 300.17 | 300.40 |  |
| $C_{12}H_{20}O_2$ | 197.1536 | 196.15 | 196.29 |  |
| $C_{12}H_{16}O_2$ | 193.1223 | 192.12 | 192.26 |  |
| $C_7H_6O_2$ | 123.0441 | 122.04 | 122.12 |  |
| $C_{10}H_{12}O_2$ | 165.0910 | 164.08 | 164.20 |  |
| $C_9H_{18}O$ | 143.1430 | 142.14 | 142.24 |  |

# References

1. D. Tang, J. Li, Z. Yang, X. Jiang, L. Huang, X. Guo, Y. Li, J. Zhu and X. Sun, Fabrication and mechanism exploration of oxygen-incorporated $1T\text{-}MoS_2$ with high adsorption performance on methylene blue, *Chemical Engineering Journal*, 2022, **428**.

2. E. C. Cho, C. W. Chang-Jian, J. H. Huang, G. Y. Lee, W. H. Hung, M. Y. Sung, K. C. Lee, H. C. Weng, W. L. Syu, Y. S. Hsiao and C. P. Chen, $Co^{2+}$-Doped $BiOBr_xCl_{1\text{-}x}$ hierarchical microspheres display enhanced visible-light photocatalytic performance in the degradation of rhodamine B and antibiotics and the inactivation of E. coli, *J Hazard Mater*, 2021, **402**, 123457.

3. S. Guan, H. Yang, X. Sun and T. Xian, Preparation and promising application of novel $LaFeO_3/BiOBr$ heterojunction photocatalysts for photocatalytic and photo-Fenton removal of dyes, *Optical Materials*, 2020, **100**.

4. D. C. Nguyen, T. L. Luyen Doan, S. Prabhakaran, D. T. Tran, D. H. Kim, J. H. Lee and N. H. Kim, Hierarchical Co and Nb dual-doped $MoS_2$ nanosheets shelled micro-$TiO_2$ hollow spheres as effective multifunctional electrocatalysts for HER, OER, and ORR, *Nano Energy*, 2021, **82**.

5. G. Wang, G. Zhang, X. Ke, X. Chen, X. Chen, Y. Wang, G. Huang, J. Dong, S. Chu and M. Sui, Direct Synthesis of Stable $1T\text{-}MoS_2$ Doped with Ni Single Atoms for Water Splitting in Alkaline Media, *Small*, 2022, **18**, e2107238.

6. J. Wu, X. Li, W. Shi, P. Ling, Y. Sun, X. Jiao, S. Gao, L. Liang, J. Xu, W. Yan, C. Wang and Y. Xie, Efficient Visible-Light-Driven $CO_2$ Reduction Mediated by Defect-Engineered BiOBr Atomic Layers, *Angew Chem Int Ed Engl*, 2018, **57**, 8719-8723.

7. Z. Lu, J. Xie, J. Hu, K. Wang and Y. Cao, In Situ Replacement Synthesis of Co@NCNT Encapsulated $CoPt_3$@$Co_2$ P Heterojunction Boosting Methanol Oxidation and Hydrogen Evolution, *Small*, 2021, **17**, e2104656.

8. R. Zhang, G. Wang, Z. Wei, X. Teng, J. Wang, J. Miao, Y. Wang, F. Yang, X. Zhu, C. Chen, E. Zhou, W. Hu and X. Sun, A Fe–$Ni_5P_4$/Fe–$Ni_2P$ heterojunction electrocatalyst for highly efficient solar-to-hydrogen generation, *Journal of Materials Chemistry A*, 2021, **9**, 1221-1229.

9. J. Kelly, G. Morrison, N. Skillen, P. Manesiotis and P. K. J. Robertson, An investigation of the role of pH in the rapid photocatalytic degradation of MCPA and its primary intermediate by low-power UV LED irradiation, *Chemical Engineering Journal*, 2019, **359**, 112-118.

10. J. He, Z. Zheng and I. M. C. Lo, Different responses of gram-negative and gram-positive bacteria to photocatalytic disinfection using solar-light-driven magnetic $TiO_2$-based material, and disinfection of real sewage, *Water Res*, 2021, **207**, 117816.

11. C.-X. Chen, S.-S. Yang, J. Ding, G.-Y. Wang, L. Zhong, S.-Y. Zhao, Y.-N. Zang, J.-Q. Jiang, L. Ding, Y. Zhao, L.-M. Liu and N.-Q. Ren, Non-covalent self-assembly

synthesis of AQ$_2$S@rGO nanocomposite for the degradation of sulfadiazine under solar irradiation: The indispensable effect of chloride, *Applied Catalysis B: Environmental*, 2021, **298**.

12. J. Ni, D. Liu, W. Wang, A. Wang, J. Jia, J. Tian and Z. Xing, Hierarchical defect-rich flower-like BiOBr/Ag nanoparticles/ultrathin g-C$_3$N$_4$ with transfer channels plasmonic Z-scheme heterojunction photocatalyst for accelerated visible-light-driven photothermal-photocatalytic oxytetracycline degradation, *Chemical Engineering Journal*, 2021, **419**.

13. S. Yang, Y. Feng, D. Gao, X. Wang, N. Suo, Y. Yu and S. Zhang, Electrocatalysis degradation of tetracycline in a three-dimensional aeration electrocatalysis reactor (3D-AER) with a flotation-tailings particle electrode (FPE): Physicochemical properties, influencing factors and the degradation mechanism, *J Hazard Mater*, 2021, **407**, 124361.

14. W. Xie, Y. Shi, Y. Wang, Y. Zheng, H. Liu, Q. Hu, S. Wei, H. Gu and Z. Guo, Electrospun iron/cobalt alloy nanoparticles on carbon nanofibers towards exhaustive electrocatalytic degradation of tetracycline in wastewater, *Chemical Engineering Journal*, 2021, **405**.

15. T. S. Bui, P. Bansal, B.-K. Lee, T. Mahvelati-Shamsabadi and T. Soltani, Facile fabrication of novel Ba-doped g-C$_3$N$_4$ photocatalyst with remarkably enhanced photocatalytic activity towards tetracycline elimination under visible-light irradiation, *Applied Surface Science*, 2020, **506**.

16. W. Zhao, Q. Dong, C. Sun, D. Xia, H. Huang, G. Yang, G. Wang and D. Y. C. Leung, A novel Au/g-$C_3N_4$ nanosheets/$CeO_2$ hollow nanospheres plasmonic heterojunction photocatalysts for the photocatalytic reduction of hexavalent chromium and oxidation of oxytetracycline hydrochloride, *Chemical Engineering Journal*, 2021, **409**.

17. X. Hu, C. Li, J. Song, S. Zheng and Z. Sun, Multidimensional assembly of oxygen vacancy-rich amorphous $TiO_2$-BiOBr-sepiolite composite for rapid elimination of formaldehyde and oxytetracycline under visible light, *J Colloid Interface Sci*, 2020, **574**, 61-73.

18. H. Wang, B. Liao, T. Lu, Y. Ai and G. Liu, Enhanced visible-light photocatalytic degradation of tetracycline by a novel hollow BiOCl@$CeO_2$ heterostructured microspheres: Structural characterization and reaction mechanism, *J Hazard Mater*, 2020, **385**, 121552.

19. Y. Dai, Y. Liu, J. Kong, J. Yuan, C. Sun, Q. Xian, S. Yang and H. He, High photocatalytic degradation efficiency of oxytetracycline hydrochloride over Ag/AgCl/$BiVO_4$ plasmonic photocatalyst, *Solid State Sciences*, 2019, **96**.

20. W. Dai, L. Jiang, J. Wang, Y. Pu, Y. Zhu, Y. Wang and B. Xiao, Efficient and stable photocatalytic degradation of tetracycline wastewater by 3D Polyaniline/Perylene diimide organic heterojunction under visible light irradiation, *Chemical Engineering Journal*, 2020, **397**.

21.    Q. Zhang, L. Jiang, J. Wang, Y. Zhu, Y. Pu and W. Dai, Photocatalytic degradation of tetracycline antibiotics using three-dimensional network structure perylene diimide supramolecular organic photocatalyst under visible-light irradiation, *Applied Catalysis B: Environmental*, 2020, **277**..